

# Nonlinear Evolution of Instabilities Between Dust and Sound Waves

Eric R. Moseley<sup>1,2\*</sup>, Jonathan Squire<sup>1,3,4</sup> & Philip F. Hopkins<sup>1,3</sup>

<sup>1</sup>TAPIR, Mailcode 350-17, California Institute of Technology, Pasadena, CA 91125, USA

<sup>2</sup>Department of Astrophysical Sciences, Princeton University, Princeton, NJ 08540, USA

<sup>3</sup>Walter Burke Institute for Theoretical Physics, Pasadena, CA 91125, USA

<sup>4</sup>Department of Physics, University of Otago, P.O. Box 56, Dunedin 9054, New Zealand

Submitted to MNRAS, September, 2018

## ABSTRACT

We study the non-linear evolution of the acoustic “Resonant Drag Instability” (RDI) using numerical simulations. The acoustic RDI is excited in a dust-gas mixture when dust grains stream through gas, interacting with sound waves to cause a linear instability. We study this process in a periodic box by accelerating neutral dust with an external driving force. The instability grows as predicted by linear theory, eventually breaking into turbulence and saturating. As in linear theory, the non-linear behavior is characterized by three regimes – high, intermediate, and low wavenumbers – the boundary between which is determined by the dust-gas coupling strength and the dust-to-gas mass ratio. The high and intermediate wavenumber regimes behave similarly to one another, with large dust-to-gas ratio fluctuations while the gas remains largely incompressible. The saturated state is highly anisotropic: dust is concentrated in filaments, jets, or plumes along the direction of acceleration, with turbulent vortex-like structures rapidly forming and dissipating in the perpendicular directions. The low-wavenumber regime exhibits large fluctuations in gas and dust density, but the dust and gas remain more strongly coupled in coherent “fronts” perpendicular to the acceleration. These behaviors are qualitatively different from those of dust “passively” driven by external hydrodynamic turbulence, with no back-reaction force from dust onto gas. The virulent nature of these instabilities has interesting implications for dust-driven winds in a variety of astrophysical systems, including around cool-stars, in dusty torii around active-galactic-nuclei, and in and around giant molecular clouds.

**Key words:** instabilities — turbulence — ISM: kinematics and dynamics — star formation: general — galaxies: formation — planets and satellites: formation

## 1 INTRODUCTION

Since its discovery by [Trumpler \(1930\)](#), astrophysical dust has been recognized as important in nearly all areas of astronomy. In addition to its extinction and scattering effects, dust dynamics are important for star and planet formation, the evolution of cool stars, stellar and AGN “feedback processes” (e.g. radiation pressure-driven winds), cooling in the ISM and protostellar disks, and chemical evolution. Because dust is a collection of (often charged) aerodynamic particles that are imperfectly coupled to the gas, its dynamics cannot be trivially related to the better understood gas dynamics.

In, for example, planetesimal formation – perhaps the best-studied astrophysical application where non-trivial dust dynamics play a crucial role – the imperfect dust-gas coupling produces phenomena such as dust “traps” (in, e.g., vortices and pressure bumps), turbulent concentration of grains, and the “streaming instability” ([Youdin & Goodman 2005](#)). It is increasingly believed that these dust-clustering mechanisms, especially the streaming instability, may resolve the decades-old problem of how to aggregate or grow grains from millimeter sizes through to planetesimals ([Youdin & Goodman 2005](#); [Bai & Stone 2010a](#); [Squire & Hopkins 2018b](#)).

A recent series of papers, [Squire & Hopkins \(2018a\)](#); [Hopkins & Squire \(2018b\)](#); [Squire & Hopkins \(2018b\)](#); [Hopkins & Squire \(2018a\)](#), demonstrated the existence of a generic super-class of instabilities that appear whenever dust moves through gas. These instabilities, termed “Resonant Drag Instabilities” (RDIs), generalize the streaming instability to a wide variety of astrophysical scenarios and systems, suggesting that dust-gas mixtures are usually unstable. RDIs typically have growth rates which are maximized at “resonant” angles and wavenumbers, where the phase velocity of some wave in the underlying gas medium (e.g., acoustic, magnetosonic, or Alfvén waves) matches that of the dust drift. In fact, a unique set of RDI sub-families appears for every possible “resonant pair” of dust and gas modes. For example, the “streaming instability” of [Youdin & Goodman \(2005\)](#) can be understood to arise due to the resonance of dust drift and gas epicyclic modes.

The purpose of this paper is to move beyond the linear analyses of [Squire & Hopkins \(2018a\)](#); [Hopkins & Squire \(2018b\)](#); [Squire & Hopkins \(2018b\)](#); [Hopkins & Squire \(2018a\)](#), and study the nonlinear regime of the RDI using numerical simulations. We consider one of the simplest setups possible: neutral dust, drifting under the influence of a constant driving force through a neutral (hydrodynamic), homogeneous gas medium. Physically, this situation can arise when the dust, but not the gas, is subject to an external force, such as radiation pressure. The gas supports undamped

\* E-mail: moseley@princeton.edu

sound waves, which can resonate with the drifting dust, destabilizing the “acoustic RDI.” The linear regime of this instability was studied in detail in [Hopkins & Squire \(2018b\)](#), but simulations are required to study the non-linear regime, including RDI-generated turbulence and orbit crossing in the dust. Although the setup is simple, it is important to understand the non-linear saturation of these instabilities because (1) they can provide fundamental insights into the behaviors of other, more complicated RDIs, and (2) the acoustic RDI may represent the fastest-growing RDI in many physical regimes and objects, including dusty cool-star (AGB or red giant) winds, dust in dense molecular clouds and cores, and the obscuring “torus” around AGN (see [Hopkins & Squire 2018a](#) for extensive discussion).

We emphasize that the setup and simulations in this work are fundamentally distinct from previous theoretical works that consider dust as a “passive” entity in an externally-turbulent medium (e.g. [Hogan et al. 1999](#); [Cuzzi et al. 2010](#); [Hopkins & Lee 2016](#); [Lee et al. 2017](#)). In such studies, the gas is unaffected by the dust, *viz.*, the momentum back-reaction of the dust on the gas is ignored, an assumption that is truly valid only in the zero dust-to-gas mass ratio limit. In contrast, this dust back-reaction is a crucial ingredient in causing RDIs, and without it, the ensuing behavior is qualitatively different.

In § 2, we introduce the equations and numerical methods; § 3 outlines some theoretical expectations. § 4 describes the results of our simulations, providing brief comparison to the theory. We conclude in § 5.

## 2 METHODS

As described above, our simulations are designed to study the basic physics of the acoustic RDI in the simplest setting possible. We thus consider a homogeneous mixture of dust and gas in a periodic box, with an external force acting on the dust only. Because of the drag between the gas and dust, this force accelerates the gas as well as the dust, driving a mean velocity offset between the two phases. The box is thus simulating a small “patch” of a dust-gas mixture being accelerated by some external force (such as radiation pressure) that acts differently upon the gas and dust.

### 2.1 Equations Solved

We directly integrate the equation of motion for a population of aerodynamic dust grains, each of which individually obeys

$$\frac{d\mathbf{v}_d}{dt} = -\frac{\mathbf{w}_s}{t_s} + \mathbf{a}, \quad (1)$$

where  $\frac{d}{dt}$  is the Lagrangian (co-moving) derivative,  $\mathbf{a}$  is the external force/acceleration,  $t_s$  is the drag coefficient or *stopping time*, and  $\mathbf{w}_s \equiv \mathbf{v}_d - \mathbf{u}_g$  is the *drift velocity*, defined as the difference between grain velocity ( $\mathbf{v}_d$ ) and gas velocity ( $\mathbf{u}_g$ ). We use angle brackets  $\langle \cdot \rangle$  to denote a volume average.

We will assume Epstein drag, with  $t_s$  given by<sup>1</sup> (see [Draine & Salpeter 1979](#))

$$t_s(\rho_g, \mathbf{w}_s) \equiv \sqrt{\frac{\pi\gamma}{8}} \frac{\rho_d^i \epsilon_d}{\rho_g c_s} \left(1 + \frac{9\pi\gamma}{128} \frac{\mathbf{w}_s^2}{c_s^2}\right)^{-1/2}, \quad (2)$$

<sup>1</sup> Technically the [Draine & Salpeter \(1979\)](#) expression is an approximation to the more general Epstein drag law, but the difference using a numerically-exact expression is completely negligible here.

where  $\rho_g$  is the gas density evaluated at the position of the grain,  $\gamma$  is the gas adiabatic index  $\partial \log P / \partial \log \rho_g$  (with  $P$  the gas pressure),  $\rho_d^i$  is the *internal* density of the grain,  $\epsilon_d$  is the grain radius, and  $c_s$  is the sound speed given by  $\sqrt{\partial P / \partial \rho_g}$ . We denote the ratio of dust to gas mass density as  $\mu \equiv \langle \rho_d \rangle / \langle \rho_g \rangle$ .

The gas obeys the usual Euler equations, but momentum conservation requires that we add the “back-reaction” term (drag force of grains on gas) to the momentum equation:

$$\rho_g \left( \frac{\partial}{\partial t} + \mathbf{u}_g \cdot \nabla \right) \mathbf{u}_g = -\nabla P + \int d^3\mathbf{v}_d f_d(\mathbf{v}_d) \frac{\mathbf{w}_s}{t_s}. \quad (3)$$

The latter term is simply the opposite of the force imparted by gas on grains, integrated over all dust grains at a given position. Here  $f_d(\mathbf{x}, \mathbf{v}_d)$  is the phase-space density distribution of dust — i.e. differential mass of grains per element  $d^3\mathbf{x} d^3\mathbf{v}_d$  — so the volumetric mass density of dust grains at a given position  $\mathbf{x}$  is  $\rho_d(\mathbf{x}) \equiv \int d^3\mathbf{v}_d f_d(\mathbf{v}_d)$ .

For this system, the grain properties are entirely specified by  $\rho_d^i \epsilon_d$  (the grain surface density). Because our primary goal is understanding the non-linear behavior of the instabilities, we will assume all grains in a given simulation have the same size, i.e. a single value of  $\rho_d^i \epsilon_d$ . In future work (in preparation) we will generalize to the more physical, but less easy-to-interpret, case of a general spectrum of grain sizes.

Critically, note that we do not make any fluid or “local terminal velocity” approximation for the dust, but integrate the trajectories of a population of grains directly. This is necessary to capture non-linear phenomena such as orbit crossings in the dust (otherwise, the non-linear outcomes would be unphysical).

### 2.2 Numerical Methods

We solve equations (1)–(3) using the multi-method code GIZMO ([Hopkins 2014](#)),<sup>2</sup> using the second-order Lagrangian finite-volume “meshless finite volume” (MFV) method for the hydrodynamics, which has been well-tested on problems involving multi-fluid instabilities and shock-capturing. We model dust using the usual “super-particle” method (e.g. [Carballido et al. 2008](#); [Johansen et al. 2009](#); [Bai & Stone 2010b](#); [Pan et al. 2011](#)), whereby the motion of each “dust particle” in the simulation follows Eq. 1, but each represents an ensemble of dust grains of size  $\epsilon_d$  (in other words, we sample some finite, computationally feasible number of grains). The numerical methods for this integration are described and tested in [Hopkins & Lee \(2016\)](#). The numerical implementation of the dust back-reaction is straightforward: in a given timestep  $\Delta t$ , one solves the coupled dust-gas equation exactly for the momentum change  $\Delta \mathbf{p}$  to a single grain super-particle moving through a (internally homogeneous) computational cell. One then subtracts that momentum from the gas cell (as for the usual hydrodynamic flux), guaranteeing momentum conservation.

The gas and dust integration capabilities of GIZMO have been extensively validated in [Hopkins \(2014\)](#) and [Hopkins & Lee \(2016\)](#). For this work, we have also run various resolution tests (see Fig. A1) and compared to analytic solutions in the linear regime of the RDI. In addition, we have run several simulations which are identical to others in our suite, except for numerical methods. Such

<sup>2</sup> A public version of the code, including all methods used in this paper, is available at <http://www.tapir.caltech.edu/~phopkins/Site/GIZMO.html>

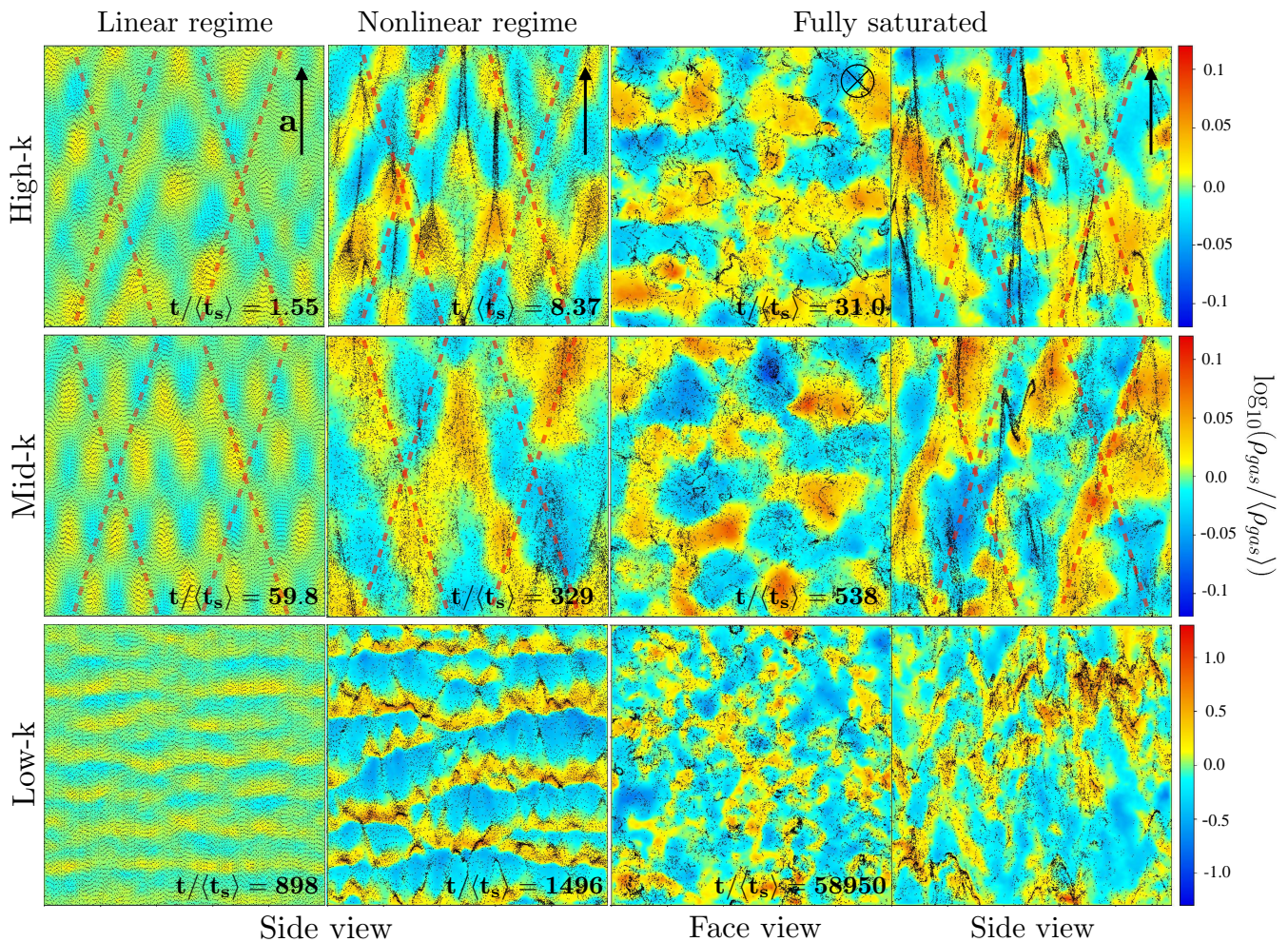


**Figure 1.** Evolution of the acoustic RDI in three representative case studies (Tab. 1) at high- $k$  (top), mid- $k$  (middle), and low- $k$  (bottom). Colors show gas density in a 2D slice through the 3D simulation box (color scale shown), with dust in slice shown as dots. Columns (1, 2, 4) show “side-on” slices (along direction of acceleration  $\mathbf{a}$ ), while column (3) shows a “face-on” slice (perpendicular to  $\mathbf{a}$ ); for clarity the direction of  $\mathbf{a}$  is labeled in the upper right corner of each column. From left-to-right, panels show evolution into turbulence (times in units of equilibrium-state dust stopping time  $\langle t_s \rangle$ ), illustrating (1) linear (or near-linear) initial evolution (modest dust & gas fluctuations); (2) the early nonlinear regime (fluctuations are regular and resemble extreme linear instabilities); (3)-(4) fully non-linear regimes (with saturated box-scale turbulence). Dust and gas density fluctuations are less (more) strongly coupled on small/high- $k$  (large/low- $k$ ) scales. Dotted lines show the predicted wavefront orientation for the fastest-growing mode angle in linear theory.

tests include (1) a different hydrodynamic solver (the meshless-finite-mass or “MFM” method), (2) a different time integration and reconstruction scheme for the grains (a less accurate cell-centered scheme), (3) different initial conditions (using a glass-like, instead of regular, initial cell configuration), (4) different box geometries (boxes more extended in the drift direction by a factor  $\sim 2 - 8$ ). These changes do not significantly affect our conclusions. We have also run a large suite of 2D simulations (reaching  $\sim 2 \times 2048^2$  resolution), which we do not present here, but produce qualitatively largely similar behavior in the dust, despite the (expected) different non-linear behavior of the induced gas turbulent cascade.

Our default simulations adopt a resolution  $N_{\text{gas}} = 128^3$  gas elements, with an equal number of dust elements  $N_{\text{dust}}$ . We have confirmed our major results with higher resolution simulations at  $N = 256^3$ , and in fact also find similar behavior in lower-resolution ( $N = 64^3$ ) simulations run for testing purposes.

### 2.3 Equilibrium Solution and Initial Conditions

In our simulations, only the dust is driven by the (constant) external radiation force ( $\mathbf{a}$ ), while the dust back-reaction on the gas acts to accelerate the gas. As discussed in detail Hopkins & Squire (2018b), this leads to a quasi-equilibrium solution where the entire dust-gas system accelerates. Simultaneously, there is also a mean velocity offset between the dust and gas that balances the drag force against the radiation force and the system’s own inertia. Because the acceleration of the system is linear and constant, the physics of the RDI in this reference frame is unchanged compared to an inertial reference frame (e.g. where either the gas or dust is stationary<sup>3</sup>). For analysis purposes, we transform back to the reference frame where the gas is stationary.

In detail, the quasi-equilibrium, steady-state solution is homo-

<sup>3</sup> To ensure numerical accuracy, we have checked this explicitly in our simulations by adding an external force to both the gas and the dust, balancing  $\mathbf{a}$  and keeping the gas stationary.

geneous, with uniform mean dust-to-gas ratio  $\mu \equiv \langle \rho_d \rangle / \langle \rho_g \rangle$ , gas velocity  $\langle \mathbf{u}_g \rangle = \langle \mathbf{u} \rangle(t=0) + \mathbf{a} t \mu / (1 + \mu)$  (i.e. constant acceleration), and dust drift  $\langle \mathbf{w}_s \rangle \equiv \langle \mathbf{v}_d \rangle - \langle \mathbf{u}_g \rangle = \mathbf{a} \langle t_s \rangle / (1 + \mu)$ . Here,  $\langle t_s \rangle = t_s(\langle \rho_g \rangle, \langle \mathbf{w}_s \rangle)$  is the stopping time at the equilibrium drift velocity, and its dependence on  $\mathbf{w}_s$  implies that the equilibrium drift velocity depends on the detailed form of the Epstein drag law, Eq. (2). From hereon, we shall denote this equilibrium value of  $\mathbf{w}_s$  as  $\mathbf{w}_{s,\text{eq}}$ , which should be distinguished from the value measured in the saturated state of a simulation  $\langle \mathbf{w}_s \rangle_{\text{sat}}$  that can differ from  $\mathbf{w}_{s,\text{eq}}$  due to the RDI-generated turbulence. Our simulations begin from these equilibrium solutions at  $t = 0$ : we initialize a 3D periodic (cubic) box of side-length  $L_0$  with uniform dust and gas densities,  $\langle \mathbf{u} \rangle(t=0) = 0$ , and  $\mathbf{v}_d = \mathbf{w}_s = \mathbf{w}_{s,\text{eq}} = \mathbf{a} \langle t_s \rangle / (1 + \mu)$  for all dust particles.

## 2.4 Units

A convenient unit system for our simulations is formed using the equilibrium gas sound speed  $\langle c_s \rangle$  and gas density  $\langle \rho_g \rangle$ , and box size  $L_0$ . In these units, the initial conditions and outcome of the simulations is (at a given resolution) entirely determined by three dimensionless parameters: the mean dust-to-gas ratio  $\mu$ , the acceleration

$$\bar{a} \equiv \mathbf{a} L_0 / \langle c_s \rangle^2, \quad (4)$$

and the grain size parameter

$$\bar{\epsilon}_d \equiv \rho_d^i \epsilon_d / \langle \rho_g \rangle L_0. \quad (5)$$

From the equilibrium solutions above, we see that these are equivalent to specifying the dimensionless equilibrium drift Mach number  $\langle \mathbf{w}_s \rangle / \langle c_s \rangle$ , the stopping time  $\langle t_s \rangle \langle c_s \rangle / L_0$ , and  $\mu$ . For convenience, we define the smallest wavenumber that can fit in the box,  $k_0 \equiv 2\pi / L_0$ .

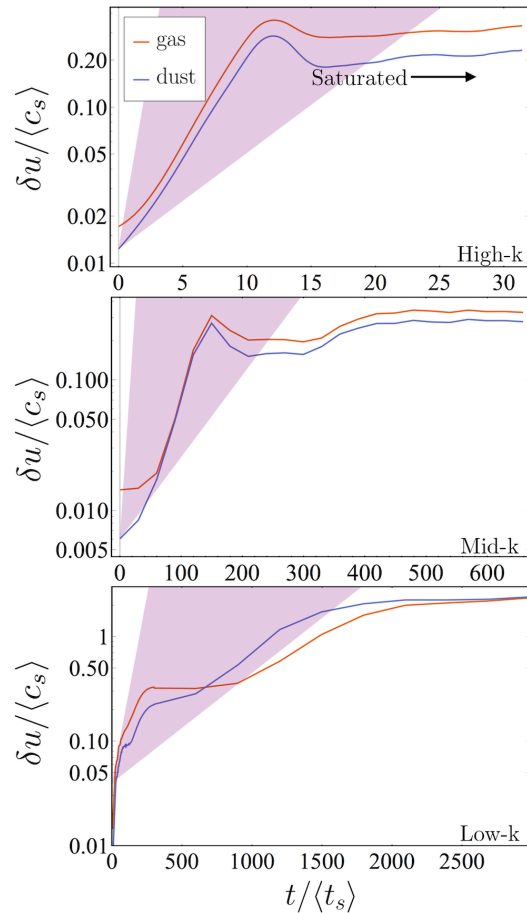
## 2.5 Simulations

Table 1 lists the ‘‘production’’ simulations that we have run as part of this study. In most simulations, the equilibrium dust drift is supersonic ( $\langle \mathbf{w}_{s,\text{eq}} \rangle / \langle c_s \rangle \gtrsim 1$ ). Although various different RDIs may be important even when the drift is highly subsonic (for example, the ‘‘streaming instability’’ and ‘‘settling instability’’ with gas epicyclic waves [Squire & Hopkins 2018b](#)), the acoustic RDI studied here grows fastest when the drift is supersonic, and we only expect it to dominate over other RDIs in this regime. Consequently, in our default simulations, we adopt an isothermal equation-of-state (EOS) for the gas ( $\gamma = 1$ ), which is appropriate for GMCs and dense, neutral gas where cooling times are short and motions are often highly supersonic (and where dust charge, which couples grains to magnetic fields, can often be neglected).<sup>4</sup>

## 2.6 Analysis

Unless otherwise noted, all statistics computed here are volume weighted. Gas statistics can be computed directly from GIZMO output, using the fact that a gas resolution element  $a$  has volume  $m_{\text{gas}}^a / \rho_{\text{gas}}^a$ . Dust statistics are computed in the same way, using the local dust density in the vicinity of each dust superparticle,  $\rho_{\text{dust}}^a$ , and the mass of the super-particle  $m_p^a = M_{\text{dust}} / N_{\text{dust}}$

<sup>4</sup> Because our default equation-of-state is isothermal, we note that  $c_s = \langle c_s \rangle$  is constant, and we can use  $c_s$  and  $\langle c_s \rangle$  interchangeably.



**Figure 2.** Time evolution of velocity dispersion in dust and gas versus time (in units of equilibrium stopping time  $\langle t_s \rangle$ ). Panels show high/mid/low- $k$  representative ‘‘case study’’ simulations as Fig. 1. In each, the shaded fan shows the range of growth rates from linear theory (Eq. 7), from wavenumbers  $k = (1 - 128) 2\pi / L_0$  (where  $N = 128$  is the linear resolution), which is consistent with the early growth rates. Statistics of the turbulence are measured in the saturated states as identified.

(where  $M_{\text{dust}} = \mu M_{\text{gas}}$  is the total dust mass in the box). Because  $\rho_{\text{dust}}^a$  is not used directly in the GIZMO calculation, it is computed in post-processing using an SPH-like local kernel density estimator:  $\rho_{\text{dust}}^a = \sum_b m_p^b W(\mathbf{x}_a - \mathbf{x}_b, H_a)$ , where  $W(\mathbf{x}_a - \mathbf{x}_b, H_a)$  is the usual cubic spline kernel with radius of compact support  $2H_a$  and  $H_a = (m_p^a / \rho_{\text{dust}}^a)^{1/3}$  is the local mean inter-particle spacing.

All simulations are run well past saturation to confirm they have reached steady-state, and all ‘‘saturated’’ quantities plotted are time-averaged across all snapshots after saturation (the exact cut used makes little difference to the values).

## 3 THEORETICAL EXPECTATIONS

### 3.1 Linear Theory: The Three Regimes

[Hopkins & Squire \(2018b\)](#) considered a linear stability analysis of the equations solved here, adopting the usual Fourier decomposition of perturbations  $\delta f \propto \exp[i(\mathbf{k} \cdot \mathbf{x} - \omega t)]$  (for some field  $f$ , such as  $\mathbf{u}_g$  or  $\rho_g$ ). They showed that the behavior of the interesting unstable solutions depended critically on the dimensionless wavenumber parameter  $k \langle c_s \rangle \langle t_s \rangle \equiv |\mathbf{k}| \langle c_s \rangle \langle t_s \rangle$  of the mode. Three

Name	$\mu \equiv \frac{\langle \rho_d \rangle}{\langle \rho_g \rangle}$	$\bar{a} \equiv \frac{ \mathbf{a}  L_0}{\langle c_s \rangle^2}$	$\bar{\epsilon}_d \equiv \frac{\rho_d^i \epsilon_d}{(\rho_g) L_0}$	Regime	$\frac{\langle c_s \rangle \langle t_s \rangle \eta}{L_0}$	$\frac{\langle w_s \rangle_{\text{sat}}}{\langle c_s \rangle}$	$\frac{\langle \delta u_{\text{gas}} \rangle_{\text{sat}}^{1/2}}{\langle c_s \rangle}$	$\sigma_{\log \rho_{\text{gas}}}^{\text{sat}}$	$\sigma_{\log \rho_{\text{dust}}}^{\text{sat}}$
$\mu 0.001\text{-}\bar{a}100\text{-}\bar{\epsilon}_d 0.1$	0.001	100	0.1	mid- <i>k</i>	0.034	3.5	0.051	0.00052	0.14
$\mu 0.001\text{-}\bar{a}1e3\text{-}\bar{\epsilon}_d 0.001$	0.001	1000	0.001	mid- <i>k</i>	0.00060	0.84	0.19	0.074	0.21
$\mu 0.001\text{-}\bar{a}1e3\text{-}\bar{\epsilon}_d 0.01$	0.001	1000	0.01	mid- <i>k</i>	0.0034	3.7	0.34	0.042	0.39
$\mu 0.001\text{-}\bar{a}1e3\text{-}\bar{\epsilon}_d 0.1$	0.001	1000	0.1	mid- <i>k</i>	0.011	12	0.13	0.030	0.19
$\mu 0.01\text{-}\bar{a}1\text{-}\bar{\epsilon}_d 0.1$	0.01	1	0.1	mid- <i>k</i>	0.063	0.063	0.013	0.00030	0.11
$\mu 0.01\text{-}\bar{a}1\text{-}\bar{\epsilon}_d 1$	0.01	1	1	mid- <i>k</i>	0.60	0.60	0.012	0.00027	0.046
$\mu 0.01\text{-}\bar{a}1\text{-}\bar{\epsilon}_d 10$	0.01	1	10	mid-high	3.3	3.3	0.013	0.00027	0.045
$\mu 0.01\text{-}\bar{a}10\text{-}\bar{\epsilon}_d 0.1$	0.01	10	0.1	mid- <i>k</i>	0.060	0.60	0.013	0.00027	0.048
$\mu 0.01\text{-}\bar{a}10\text{-}\bar{\epsilon}_d 1$	0.01	10	1	mid- <i>k</i>	0.33	3.3	0.097	0.0030	0.31
$\mu 0.01\text{-}\bar{a}100\text{-}\bar{\epsilon}_d 0.01$	0.01	100	0.01	mid- <i>k</i>	0.0060	0.73	0.12	0.034	0.13
$\mu 0.01\text{-}\bar{a}100\text{-}\bar{\epsilon}_d 0.1\text{-}LR$	0.01	100	0.1	mid- <i>k</i>	0.033	3.3	0.35	0.028	0.071
<b><math>\mu 0.01\text{-}\bar{a}100\text{-}\bar{\epsilon}_d 0.1</math></b>	<b>0.01</b>	<b>100</b>	<b>0.1</b>	<b>mid-<i>k</i></b>	<b>0.033</b>	<b>3.3</b>	<b>0.33</b>	<b>0.025</b>	<b>0.37</b>
$\mu 0.01\text{-}\bar{a}100\text{-}\bar{\epsilon}_d 0.1\text{-}HR$	0.01	100	0.1	mid- <i>k</i>	0.033	3.3	0.32	0.033	0.43
$\mu 0.01\text{-}\bar{a}1e3\text{-}\bar{\epsilon}_d 0.001$	0.01	1000	0.001	low-mid	0.00060	0.85	0.53	0.14	0.23
$\mu 0.01\text{-}\bar{a}1e3\text{-}\bar{\epsilon}_d 0.1$	0.01	1000	0.1	mid- <i>k</i>	0.011	11.8	0.88	0.063	0.37
$\mu 0.01\text{-}\bar{a}1e3\text{-}\bar{\epsilon}_d 0.1\text{-}\gamma 5/3$	0.01	1000	0.1	mid- <i>k</i>	0.012	10	0.69	0.032	0.26
$\mu 0.01\text{-}\bar{a}1e3\text{-}\bar{\epsilon}_d 1$	0.01	1000	1	mid- <i>k</i>	0.036	37	0.51	0.024	0.17
$\mu 0.01\text{-}\bar{a}1e4\text{-}\bar{\epsilon}_d 0.001\text{-}LR$	0.01	10000	0.001	low- <i>k</i>	0.00033	4.6	3.5	0.20	0.33
<b><math>\mu 0.01\text{-}\bar{a}1e4\text{-}\bar{\epsilon}_d 0.001</math></b>	<b>0.01</b>	<b>10000</b>	<b>0.001</b>	<b>low-<i>k</i></b>	<b>0.00033</b>	<b>4.6</b>	<b>3.4</b>	<b>0.22</b>	<b>0.40</b>
$\mu 0.01\text{-}\bar{a}1e4\text{-}\bar{\epsilon}_d 0.001\text{-}HR$	0.01	10000	0.001	low- <i>k</i>	0.00033	4.2	3.0	0.23	0.43
$\mu 0.01\text{-}\bar{a}1e4\text{-}\bar{\epsilon}_d 0.1$	0.01	10000	0.1	mid- <i>k</i>	0.0036	37	20	0.19	0.50
$\mu 0.01\text{-}\bar{a}1e5\text{-}\bar{\epsilon}_d 0.1$	0.01	100000	0.1	low-mid	0.0011	100	127	0.32	0.55
$\mu 0.01\text{-}\bar{a}1e6\text{-}\bar{\epsilon}_d 0.001$	0.01	1000000	0.001	low- <i>k</i>	0.000036	44	94	0.29	0.40
$\mu 0.1\text{-}\bar{a}1\text{-}\bar{\epsilon}_d 10$	0.1	1	10	high- <i>k</i>	3.2	3.0	0.013	0.00027	0.046
$\mu 0.1\text{-}\bar{a}10\text{-}\bar{\epsilon}_d 0.1$	0.1	10	0.1	mid- <i>k</i>	0.060	0.55	0.013	0.00027	0.050
<b><math>\mu 0.1\text{-}\bar{a}10\text{-}\bar{\epsilon}_d 1</math></b>	<b>0.1</b>	<b>10</b>	<b>1</b>	<b>mid-high</b>	<b>0.32</b>	<b>3.2</b>	<b>0.33</b>	<b>0.021</b>	<b>0.46</b>
$\mu 0.1\text{-}\bar{a}10\text{-}\bar{\epsilon}_d 10$	0.1	10	10	mid-high	1.1	2.2	0.76	0.047	0.32
$\mu 0.1\text{-}\bar{a}100\text{-}\bar{\epsilon}_d 0.1$	0.1	100	0.1	mid- <i>k</i>	0.032	3.2	1.6	0.11	0.45
$\mu 0.1\text{-}\bar{a}1e3\text{-}\bar{\epsilon}_d 0.001$	0.1	1000	0.001	low- <i>k</i>	0.00060	0.86	1.8	0.16	0.20
$\mu 0.1\text{-}\bar{a}1e3\text{-}\bar{\epsilon}_d 0.1$	0.1	1000	0.1	low-mid	0.011	2.4	32	0.17	0.51
$\mu 1\text{-}\bar{a}10\text{-}\bar{\epsilon}_d 0.1$	1	10	0.1		0.056	0.37	1.1	0.079	0.41
$\mu 1\text{-}\bar{a}100\text{-}\bar{\epsilon}_d 0.1$	1	100	0.1		0.025	1.9	8.2	0.12	0.43
$\mu 1\text{-}\bar{a}1e3\text{-}\bar{\epsilon}_d 0.001$	1	1000	0.001		0.00056	0.54	6.9	0.24	0.26
$\mu 1\text{-}\bar{a}1e3\text{-}\bar{\epsilon}_d 0.1$	1	1000	0.1		0.0081	11	58	0.22	0.86
$\mu 10\text{-}\bar{a}100\text{-}\bar{\epsilon}_d 0.1$	10	100	0.1		0.011	1.1	6.1	0.1	0.33
$\mu 10\text{-}\bar{a}1e3\text{-}\bar{\epsilon}_d 0.001$	10	1000	0.001		0.00032	0.14	1.4	0.16	0.15
$\mu 10\text{-}\bar{a}1e3\text{-}\bar{\epsilon}_d 0.1$	10	1000	0.1		0.0034	3.6	15	0.18	0.38
$\mu 100\text{-}\bar{a}10\text{-}\bar{\epsilon}_d 0.1$	100	10	0.1		0.011	0.13	0.24	0.025	0.13
$\mu 100\text{-}\bar{a}100\text{-}\bar{\epsilon}_d 0.1$	100	100	0.1		0.0036	0.19	1.1	0.15	0.27
$\mu 100\text{-}\bar{a}1e3\text{-}\bar{\epsilon}_d 0.1$	100	1000	0.1		0.0011	0.86	1.6	0.20	0.20

**Table 1.** Simulations studied here. We denote: (1) Simulation name. (2) Total dust-to-gas mass ratio  $\mu$ . (3) Differential acceleration  $\mathbf{a}$  imposed between dust and gas (in dimensionless units of box size  $L_0$  and isothermal sound speed  $\langle c_s \rangle$ ). (4) Dimensionless grain size/surface density parameter  $\bar{\epsilon}_d$ , which determines the strength of the drag forces. (5) Regime of the simulation (low, mid, or high-*k*, or a mix), calculated from the largest 6 modes in the box for simulations with  $\mu < 1$ . (6) Initial stopping time (drag coefficient)  $t_s$  of grains in the homogeneous equilibrium setup: the ratio  $c_s t_s / L_0$  defines the “low”-*k* vs. “mid”/“high”-*k* regimes. (7) Mean drift velocity of grains relative to gas  $\langle w_s \rangle$ , measured in the saturated turbulent state – especially large values indicate systems where grains “draft” through narrow channels carved in the gas. (8) Volume-weighted standard-deviation of gas velocity in the box, measured in the saturated state. (9) Volume-weighted standard-deviation of logarithmic gas density ( $\log_{10}(\rho_g / \langle \rho_g \rangle)$ ), again measured in the saturated state. (10) Same for dust density. Bold names denote the “case studies” used in Figs. 1–6. Gray names indicate that the simulation is likely affected by the numerical issues discussed in App. A.

regimes emerge:

$$\begin{cases} k \langle c_s \rangle \langle t_s \rangle \lesssim \mu & (\text{Low-}k), \\ \mu \lesssim k \langle c_s \rangle \langle t_s \rangle \lesssim \mu^{-1} & (\text{Mid-}k), \\ k \langle c_s \rangle \langle t_s \rangle \gtrsim \mu^{-1} & (\text{High-}k). \end{cases} \quad (6)$$

The linear behavior of the mid-*k* and high-*k* regimes is qualitatively similar, albeit with somewhat different scalings for the growth rates and mode structure. In both cases the fastest-growing modes are those that are “resonant,” with  $\hat{\mathbf{k}} \cdot \langle \mathbf{w}_s \rangle = \pm c_s$ , i.e. with the drift velocity in the direction of the mode matching the sound speed. We can also see above that as  $\mu \rightarrow 0$ , the mid-*k* regime extends to all *k*; it is therefore also the “low- $\mu$ ” regime.

In the low-*k* regime, in contrast, the fastest-growing mode is

the so-called “pressure-free” mode. In this regime, the bulk force from dust on gas becomes larger than pressure forces, so the gas becomes highly compressible, and the fastest-growing modes are those with  $\hat{\mathbf{k}}$  aligned with  $\mathbf{a}$  (or  $\langle \mathbf{w}_s \rangle$ ).

The linear growth rates of the fastest-growing modes in each regime are approximately given by (Hopkins & Squire 2018b),

$$\Im(\omega) \langle t_s \rangle \sim \begin{cases} \mu^{1/3} (k \langle c_s \rangle \langle t_s \rangle)^{2/3} (\langle w_s \rangle / c_s)^{2/3} & (\text{Low-}k), \\ \mu^{1/2} (k \langle c_s \rangle \langle t_s \rangle)^{1/2} & \text{at } \langle w_s \rangle > c_s \quad (\text{Mid-}k), \\ \mu^{1/3} (k \langle c_s \rangle \langle t_s \rangle)^{1/3} & \text{at } \langle w_s \rangle > c_s \quad (\text{High-}k), \end{cases} \quad (7)$$

where here  $\langle w_s \rangle$  and other quantities refer, of course, to their values in the equilibrium, homogeneous solution. In Eqs. (6)–(7) we simplified by taking  $\mu \ll 1$ , which is chosen for most of the cases

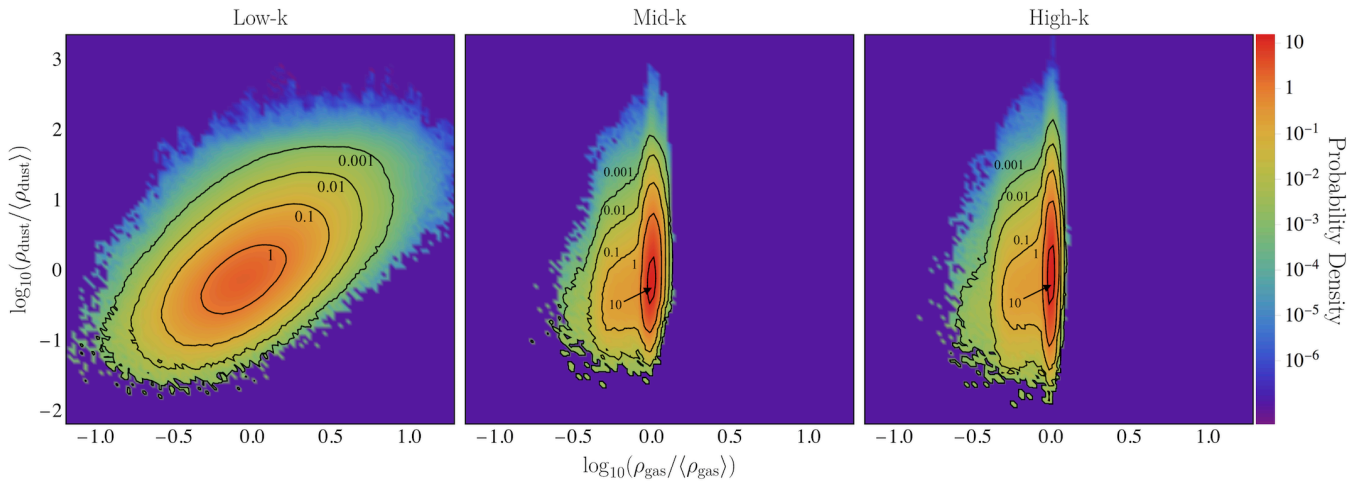


**Figure 3.** Volume-weighted joint probability density function (PDF) of gas and dust density for the simulations in Fig. 1. At low- $k$ , dust and gas are relatively well-correlated. At mid/high- $k$ , an asymmetric PDF develops where gas develops a long tail at low densities (characteristic of subsonic turbulence), while dust remains relatively symmetric with a much larger density dispersion.

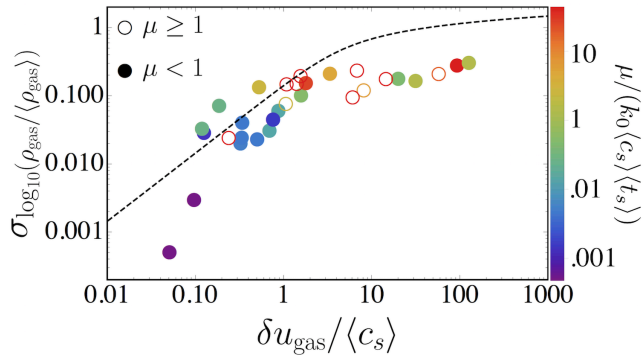


**Figure 4.** Standard deviation of logarithmic gas density, versus gas velocity dispersion. Plotted line is the standard scaling from Federrath et al. (2008) with  $b = 1/3$ . This provides a reasonable fit for  $\delta u_{\text{gas}} \ll 3 c_s$ , but the simulations here produce weaker density fluctuations when  $\delta u_{\text{gas}} \gtrsim 3 c_s$ , as these extreme cases tend to involve gas moving rapidly with dust along “channels” (rather than e.g. isotropic compressible turbulence in the gas).

we consider here due to its greater astrophysical relevance. Growth rates for subsonic drift ( $\langle w_s \rangle < c_s$ ) in the mid- and high- $k$  regimes are significantly lower and depend on details of the equation of state and dust drag (Hopkins & Squire 2018b). From Eqs. (4)–(5) or Tab. 1 (see column 4, which lists  $\langle c_s \rangle \langle t_s \rangle / L_0$ ), we see that simulations with smaller (larger)  $\bar{\epsilon}_d$  or larger (smaller)  $\bar{a}$  will have smaller (larger) dimensionless wavenumbers  $k \langle c_s \rangle \langle t_s \rangle$ .

### 3.2 Expected Turbulent Scalings

Here we give simple, quasi-linear estimates for the amplitude of the turbulence driven by the acoustic RDI. We see below (§ 4) that these match the measured saturated states of the simulations relatively well.

The basic idea of the argument is to match the turnover time of the turbulence on the largest scale in the box to the growth rate of the RDI. Given the predicted growth rates  $\Im(\omega)$ , and assuming that the saturated state is turbulent, then when the turnover time of the largest eddies is smaller than their growth time  $1/\Im(\omega)$ , all scales in the box are mixed before they can grow. Thus, a reasonable es-

timate for the saturation amplitude of RDI generated turbulence is when  $t_{\text{eddy}}^{-1} \sim k_0 \delta u_{\text{gas}} \sim k_0 \delta v_{\text{dust}} \sim \Im(\omega)$ , giving,

$$\frac{\delta u_{\text{gas}}}{c_s} \sim \begin{cases} \mu^{1/3} (\langle w_s \rangle / c_s)^{2/3} (k_0 \langle c_s \rangle \langle t_s \rangle)^{-1/3} & \text{(Low-}k\text{)} \\ \mu^{1/2} (k_0 \langle c_s \rangle \langle t_s \rangle)^{-1/2} & \text{(Mid-}k\text{)} \\ \mu^{1/3} (k_0 \langle c_s \rangle \langle t_s \rangle)^{-2/3} & \text{(High-}k\text{)}. \end{cases} \quad (8)$$

Combining the regime definitions (Eq. 6) with these expressions, we see that the mid- $k$  and high- $k$  regimes can generate only subsonic gas turbulence when  $\mu < 1$ , with  $\mu^{1/2} \lesssim \delta u_{\text{gas}} / c_s \lesssim 1$  in the mid- $k$  regime, and  $\delta u_{\text{gas}} / c_s \lesssim \mu$  in the high- $k$  regime. In contrast, turbulence generated by the low- $k$  mode can be supersonic in the gas for sufficiently low  $k$  or high  $\langle w_s \rangle / c_s$  (with  $\delta u_{\text{gas}} / c_s \gtrsim (\langle w_s \rangle / c_s)^{2/3}$ ).

From this, we can speculate further about gas density statistics. In isothermal turbulence, the gas develops an approximately log-normal density distribution with variance  $\sigma^2(\log_{10} \rho) \approx (\ln 10)^{-2} \ln [1 + (b \delta u_{\text{gas}} / c_s)^2]$  where  $b \sim 1/4 - 1$ , depending on the forcing (e.g. Federrath et al. 2008). From the above (and assuming  $b \sim 1/3$ ), we obtain, for the mid- $k$  and high- $k$  regimes,  $\sigma(\log_{10} \rho) \sim 0.1 (\delta u_{\text{gas}} / c_s)$  (which is  $\ll 1$  always). For the low- $k$  regime, we obtain  $\sigma(\log_{10} \rho)$ , which can be larger but (because of the logarithmic suppression) should lie between  $\sim 0.1 - 0.6$  for all parameters simulated here.

In a saturated state, it is reasonable to assume that dust and gas are well mixed and efficiently share energy locally (with respect to the local mean drift), implying that that two should have similar velocity dispersions,  $\delta v_{\text{dust}} \sim \delta u_{\text{gas}}$ . However, the corresponding dust density fluctuations are more difficult to predict, because the dust is pressure-free, meaning its density fluctuations need not be linked straightforwardly to its velocity dispersion. A detailed theory of dust fluctuations in saturated RDI turbulence will be explored in future work.

## 4 RESULTS

### 4.1 Representative Case Studies

We find that the three regimes from linear theory extend to describe many features of the nonlinear saturation as well, so we

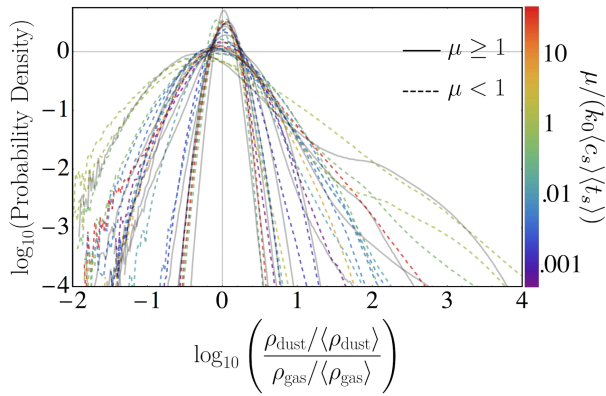


**Figure 5.** PDFs of the ratio of dust density to gas density (normalized) for all simulations. Simulations with  $\mu < 1$  are colored as labeled, those with  $\mu > 1$  are grey (since they should not obey the same scalings). Roughly, simulations with lower  $k_0 \langle c_s \rangle / \mu$  (more strongly in the “low- $k$ ” regime) have wider PDFs (expected per Fig. 7). For mid/high- $k$  regimes the PDF of  $\rho_d$  is nearly identical to  $\rho_d / \rho_g$ , since the gas is nearly-incompressible, while for the low- $k$  regime the PDF of  $\rho_d / \rho_g$  (here) is narrower than  $\rho_d$  or  $\rho_g$  alone since they fluctuate partially in phase.

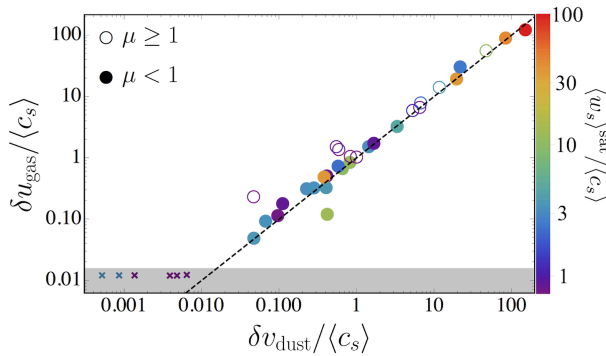


**Figure 6.** Gas vs. dust velocity dispersions, with the dashed black line being equivalence. In saturation, the two are comparable with relatively small scatter. In most cases, the mean/bulk drift velocity  $\langle w_s \rangle / \langle c_s \rangle$  of the saturated state (colors, as labeled) does not correlate strongly with the fluctuations  $\delta u_{\text{gas}}$ ,  $\delta v_{\text{dust}}$  in either dust or gas. The most extreme cases, however, do have large fluctuations *and* large drift velocities. The six simulations marked by “x”s in the bottom left failed to go turbulent due to reasons discussed in § A. They reside within a grayed out, numerically limited region. They are also listed and grayed out in Tab. 1.

frame our discussion around these. Every simulation box contains a range of wavenumbers, of course, but given our finite resolution, it is typically the case that most of the resolved modes with  $2\pi/L_0 \lesssim k \lesssim 1/\Delta x$  (where  $\Delta x \equiv L_0/N^{1/3}$  is the grid scale) lie in one particular regime for a given run. We therefore identify one simulation primarily within each regime ( $\mu 0.01\text{--}\bar{a}1e4\text{--}\bar{e}_d 0.001$ ,  $\mu 0.01\text{--}\bar{a}100\text{--}\bar{e}_d 0.1$ , and  $\mu 0.1\text{--}\bar{a}10\text{--}\bar{e}_d 1$ ) as representative of those in our parameter survey (although the largest modes of  $\mu 0.1\text{--}\bar{a}10\text{--}\bar{e}_d 1$  lie in the mid- $k$  regime, due to numerical difficulties in capturing the high- $k$  instability; see App. A).

#### 4.1.1 Linear growth of the instability

At early times, the acoustic RDI behaves as predicted in Hopkins & Squire (2018b). As seen in the first column of Figure 1, the instability begins as sinusoidal oscillations, with the dominant (fastest-

growing) wavevector clearly aligned along a characteristic angle. For the mid- $k$  and high- $k$  modes this is the predicted “resonant angle” ( $\hat{\mathbf{k}} \cdot \langle \mathbf{w}_s \rangle = \pm c_s$ ), while for the low- $k$  this is aligned with the drift  $\hat{\mathbf{k}} \parallel \langle \mathbf{w}_s \rangle$ , as expected.

Further, as seen in Figure 2, the growth rate of the instabilities at early times agrees well with the linear theory predictions assuming a fastest-growing<sup>5</sup> wavenumber  $k_{\text{max}}$  between  $\sim 1/\Delta x$  and  $\sim 3/\Delta x$ . The gas velocity and density fluctuations in the mid- and high- $k$  cases grow at approximately this rate until saturation, perhaps not surprising since they saturate in a quasi-linear regime. In the low- $k$  case the growth rates slow down, but do not vanish, as the perturbations become more strongly non-linear ( $\delta u_{\text{gas}}/c_s \rightarrow 1$ ).

In all cases the dust density perturbations, which do not incur any restoring pressure forces, become strongly non-linear well before the gas. This can be clearly seen in the second column of Figure 1.

Note that in certain simulations at high  $k$  and low  $\mu$  – e.g.  $\mu 0.01\text{--}\bar{a}1\text{--}\bar{e}_d 10$  – the instability does not grow as expected from linear theory, which we attribute to numerical difficulties associated with resolving the resonant angle. This is explained in more detail in App. A. Certain other simulations (e.g.  $\mu 0.01\text{--}\bar{a}1\text{--}\bar{e}_d 0.1$ ), which are at mid- or high- $k$  but with subsonic dust drift ( $\langle w_s \rangle < c_s$ ), remain laminar because the RDI is stable, or has very low growth rates, at these parameters.

#### 4.1.2 Dust and gas distributions

Figures 3 and 5 show the distributions of dust and gas (time-averaged in the saturated state). In the low- $k$  regime, dust and gas densities remain broadly proportional to one another in saturated state, even as they vary over  $\sim 1 - 2$  dex together (albeit with a  $1\sigma$  dispersion of  $\sim 0.3 - 0.6$  dex at fixed  $\rho_g$ ). This agrees with our expectation that the gas is effectively highly-compressible and moves with the dust at these wavenumbers.<sup>6</sup>

In contrast, at mid and high- $k$ , the gas is largely incompressible (with a small range in  $\rho_g$ , as expected from our arguments above), while the dust occupies a range of densities remarkably similar to the low- $k$  case. This results in larger dust-to-gas ratio fluctuations. Interestingly the “tail” of the gas density PDF to lower  $\rho_g$  typically corresponds to regions “carved out” by dense dust plumes or filaments.

Note that in simulations that lie near the “border” between the low- $k$  and mid- $k$  regimes, the joint gas-dust PDFs show the skewed shape of the incompressible high- $k$  PDF, but with some elongation in  $\rho_g$  correlated with  $\rho_d$  as in the low- $k$  PDF.

The one-dimensional PDFs of  $\rho_d/\rho_g$  are shown in Fig. 5. Because fluctuations in  $\rho_d$  are larger (especially in the mid- $k$  and high- $k$  regimes), this is similar in shape to a PDF of  $\rho_d$ . Note the distri-

<sup>5</sup> Note, because the predicted growth rates of this instability increase without limit with  $k$ , the fastest-growing mode will always be the smallest resolved. So this is not exactly defined, but occurs at some multiple of the grid scale.

<sup>6</sup> As discussed in Hopkins & Lee (2016), it is well-known that the standard numerical method of integrating trajectories of a finite number of “super-particles” can produce some numerical or “sampling” noise in the ratio  $\rho_d/\rho_g$ ; there we show this is at the level of  $\sim 0.05$  dex even when the gas is externally stirred with  $\delta u_{\text{gas}}/c_s \sim 10$  (the noise is still smaller for sub-sonic flows). This is negligible for any simulation here which develops non-laminar behavior (note the effects on  $\delta u_{\text{gas}}$  and  $\sigma(\log_{10}(\rho_g))$  are much smaller still,  $< 0.01$  dex).

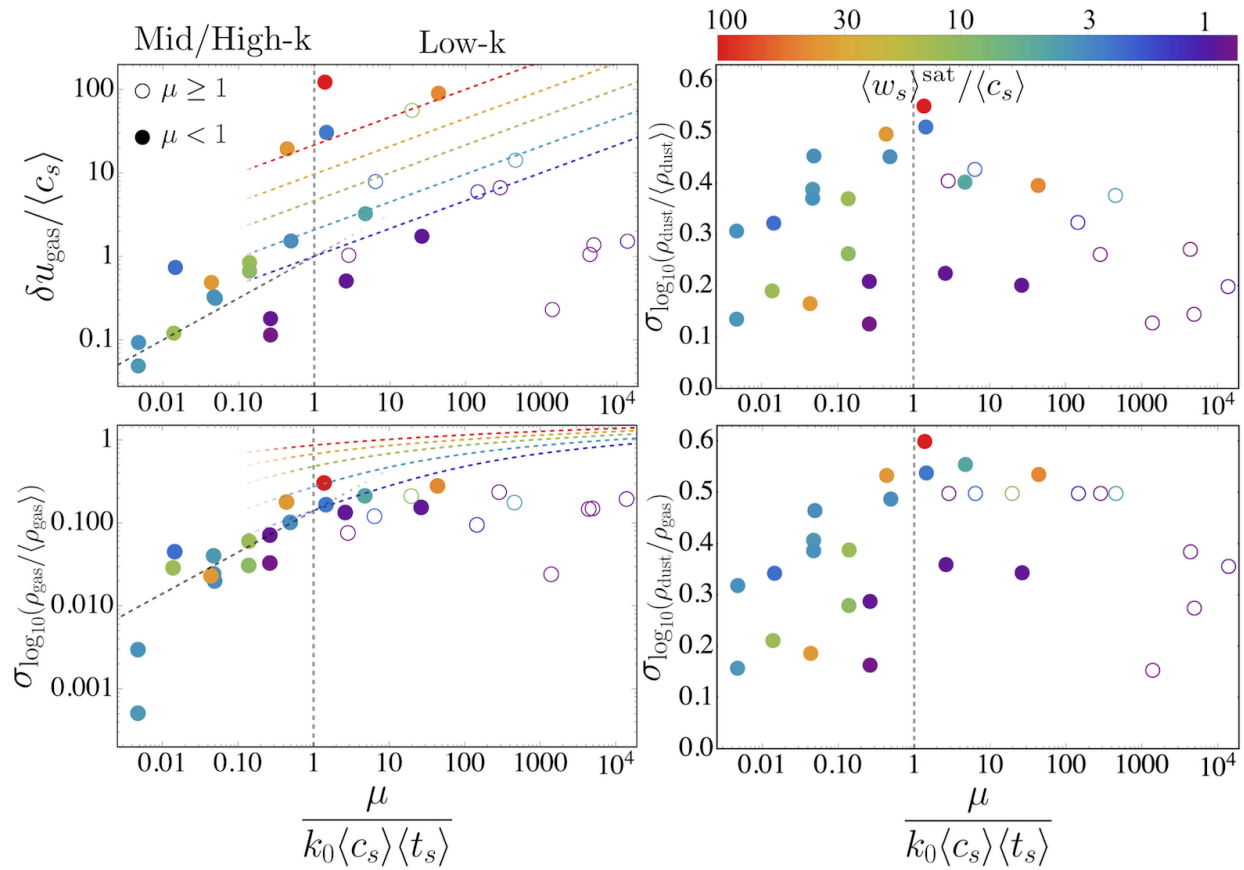


**Figure 7.** Standard deviation of gas velocity, (log) gas density, dust density, and dust-to-gas mass ratio vs.  $\mu/(k_0\langle c_s \rangle t_s)$ .  $\mu/(k_0\langle c_s \rangle t_s)$  divides the mid/low- $k$  regimes at unity, and the mid/high- $k$  regimes at  $\mu/(k_0\langle c_s \rangle t_s) = \mu^2$ . *Top Left:* Dotted lines compare the quasi-linear theory prediction (§ 3), which provides a remarkably good fit except when  $\mu \gg 1$  (where several of the assumptions there break down). Note that the prediction depends on  $\langle w_s \rangle^{\text{sat}} / \langle c_s \rangle$  in the low- $k$  regime (hence separate lines for different values of  $\langle w_s \rangle^{\text{sat}} / \langle c_s \rangle$ , colored as labeled), but does not in the mid/high- $k$  regime, a feature that also appears to be present in the simulation data for  $\langle \delta u_{\text{gas}}^2 \rangle^{\text{sat}} / c_s^2$ . Large velocity fluctuations are produced at low- $k$  and large  $\langle w_s \rangle^{\text{sat}} / \langle c_s \rangle$ . The dust velocity scales similarly, per Fig. 6. *Bottom Left:* Dotted lines show the predicted  $\delta u_{\text{gas}}$ , convolved with the analytic relation for  $\sigma(\log_{10}(\rho_{\text{gas}}))$  from Fig. 4. Larger velocity fluctuations correlate with larger density fluctuations. *Top Right:* Dust density fluctuations. There is no obvious predictive relation for the pressure-free dust-density fluctuations. *Bottom Right:* Dust-to-gas-ratio fluctuations. These largely trace the  $\rho_d$  fluctuations, but are weaker at low- $k$  than would be expected in the case of dust and gas being strictly uncorrelated. That is to say, we observe  $\sigma(\log_{10}(\rho_{\text{dust}}/\rho_{\text{gas}}))^2 < \sigma(\log_{10}(\rho_{\text{dust}}/\rho_{\text{dust}}))^2 + \sigma(\log_{10}(\rho_{\text{gas}}/\rho_{\text{gas}}))^2$  at low- $k$  due to some non-zero covariance between dust and gas density.

bution is very crudely lognormal-like, but closer to a power-law in the tails at high  $\rho_d/\rho_g$ , and quite strongly skewed.

#### 4.1.3 Comparison to “Passive Dust” Simulations

Comparing the bivariate PDFs in Figure 3 to those for simulations of “passive” dust clustering in externally-driven isothermal turbulence in Hopkins & Lee (2016)<sup>7</sup> (see also Pan & Padoan 2013; Hogan et al. 1999; Lee et al. 2017), it is clear that the PDFs for the mid- $k$  and high- $k$  regimes here are qualitatively different from the PDFs in those “passive dust” experiments, at any turbulent Mach number.

Even the low- $k$  PDF, which broadly resembles some “passive dust” cases at higher Mach number, differs qualitatively in detail. For example, in passive dust simulations (see, e.g. figure 9 of Hopkins & Lee 2016), the bivariate PDF always tapers noticeably to  $\rho_d \approx \mu \rho_g$  as  $\rho_g$  increases, because the dust is more tightly coupled

to the gas in dense regions. Here, as seen in the left-hand panel of Fig. 3, the opposite occurs, because the RDI operates on all density scales and it is the dust that *drives* the large density fluctuations in the first place.

Moreover, the global, strong anisotropy of RDI turbulence is clear in all regimes in Fig. 1, and is quite different from externally-driven turbulence. Specifically, the dust is arranged into filaments with a preferred direction along the characteristic mode angles of the RDI, even in the nonlinear, turbulent state. Likewise, the dust morphology is quite different, with “plumes” and “jets” of dust as opposed to ridge-lines between gas vortices.

We have also confirmed these conclusions directly by running a simulation with parameters otherwise identical to an RDI simulation, but with “passive” dust ( $\mu \rightarrow 0$ ), and externally-driven turbulence tuned to produce the same  $\delta u_{\text{gas}}/c_s$  as the RDI run (using the turbulent-driving scheme of Hopkins & Lee 2016). As expected, the bivariate PDFs, morphology, anisotropy, and other key properties have almost nothing in common.

Not surprisingly, higher-order diagnostics (e.g. dust-dust and dust-gas correlation functions) differ even more dramatically be-

<sup>7</sup> Note that Hopkins & Lee (2016) used the same simulation code/numerical methods, and analysis methods.

tween RDI- and externally driven turbulence simulations. These will be studied in detail in future work.

## 4.2 Nonlinear/Saturated Scalings

Figure 7 shows the saturated values of  $\delta u_{\text{gas}}/c_s$ , for our full set of simulations. We compare to the predicted mid- $k$  and low- $k$  scalings from § 3 (Eq. 8), which do a surprisingly good job explaining the non-linear behavior, at least at the order-of-magnitude level.<sup>8</sup> It is worth noting that the mass-weighted statistics conform better to the scalings, but for consistency with the rest of the figures we have chosen to display volume-weighted statistics. Our low- $k$  scalings, while holding broadly, have a large scatter for  $\delta u_{\text{gas}}/c_s$ . The predictions for  $\sigma[\log_{10}(\rho_g/\langle\rho_g\rangle)]$  are somewhat too high at low- $k$ , although they are more accurate for the mid- and high- $k$  regimes. This is reflective of an apparent plateau in  $\sigma[\log_{10}(\rho_g/\langle\rho_g\rangle)]$  at  $\sigma[\log_{10}(\rho_g/\langle\rho_g\rangle)] \sim 0.2$  (see also Fig. 4). Figure 6 compares the saturated dust and gas velocity dispersions. As expected from equipartition arguments,  $\delta v_{\text{dust}} \approx \delta u_{\text{gas}}$  in nearly all simulations.

We did not have an *a priori* prediction for the magnitude of dust density fluctuations ( $\sigma[\log_{10}(\rho_d)]$  or  $\sigma[\log_{10}(\rho_d/\rho_g)]$ , which are similar), but Figure 7 shows they increase both with  $\mu/(k\langle c_s\rangle\langle t_s\rangle)$  and  $\langle w_s\rangle/c_s$ , reaching a maximum of  $\sim 0.5 - 0.6$  dex dispersion.

## 4.3 Extreme Cases: Decoupling of Dust “Jets”

In extreme, high-Mach-number simulations, we observe a phenomenon we term “dust drafting,” where dust aligns into narrow filaments in the direction of motion. These filaments effectively decouple from the surrounding gas, pushing the gas in a narrow cylinder out of their path. They thus accelerate with little gas resistance and achieve much higher velocities than dust outside the drafting filament. We have observed this phenomenon only for simulations with  $\mathbf{w}_{s,\text{eq}}/c_s \gtrsim 10$ , and the onset is more rapid at higher  $\mu$ . Figure 8 shows one example:  $\mu 0.01\text{-}\bar{a}1\text{e}5\text{-}\bar{e}_d 0.1$ , with  $\mathbf{w}_{s,\text{eq}}/c_s \sim 100$ , the highest in all our simulations. Because the dust has decoupled from the gas, the mass-weighted  $\langle w_s \rangle$  (termed  $\langle w_s \rangle_{\text{mass}}$ ) continues to grow indefinitely (reaching  $\langle w_s \rangle_{\text{mass}}/c_s \sim 400$  at the time shown), while the volume-weighted  $\langle w_s \rangle$  (termed  $\langle w_s \rangle_{\text{vol}}$ ) is approximately constant. The density statistics remain stable as this happens, while  $\delta u_{\text{gas}}/c_s$  continues to marginally increase.

Of course, this phenomenon is partly an artifact of using a finite, periodic simulation domain. In a global simulation with more realistic dust physics, these filaments might be driven out of the gas altogether, or trigger the onset of secondary effects like dust self-shielding and/or grain collisions.

## 4.4 Effects of the Gas Equation-of-State

Our default simulations adopt an isothermal equation-of-state (EOS) for the reasons discussed above (§ 2). However we have also re-run the simulation  $\mu 0.01\text{-}\bar{a}1\text{e}3\text{-}\bar{e}_d 0.1$  using a strictly polytropic (constant-entropy) EOS with  $P = \gamma^{-1} \langle c_s \rangle^2 \langle \rho_g \rangle (\rho_g/\langle \rho_g \rangle)^\gamma$ , with  $\gamma = 5/3$  (this is labeled with the suffix “- $\gamma 5/3$ ” in Tab. 1). Note that we effectively assume that the gas reverts instantaneously to

<sup>8</sup> Performing a maximum likelihood fit to the data in each regime, modeling  $\delta u_{\text{gas}}/c_s \propto \mu^{\alpha_\mu} (k\langle c_s \rangle\langle t_s \rangle)^{\alpha_k} (\langle w_s \rangle/c_s)^{\alpha_w}$ , we find “best-fit” power-laws consistent with our predicted scaling within the  $\sim 1\sigma$  range, but with large uncertainties arising from the limited statistics.

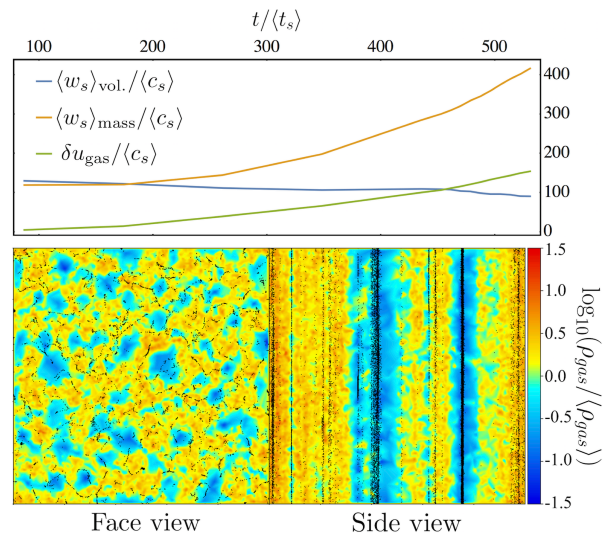


**Figure 8.** Dust drafting in simulation  $\mu 0.01\text{-}\bar{a}1\text{e}5\text{-}\bar{e}_d 0.1$ . *Top:* Volume and mass-weighted dust drift velocities ( $\langle w_s \rangle$ ) and gas velocity dispersion ( $\delta u_{\text{gas}}$ ) versus time. *Bottom:* Face/side-on slices of the simulation (as Fig. 1). When  $\langle w_s \rangle$  and  $\mu$  are sufficiently large, dust aligns into columns along the acceleration direction  $\mathbf{a}$ , with particles drafting (those upstream breaking the wind for those downstream, lowering the effective drag from gas in the filaments). This allows the dust to reach very high relative speed  $w_s$  in the filaments, and they become increasingly concentrated (and detached from the gas) with time. This means the mass-weighted  $\langle w_s \rangle_{\text{mass}}/c_s$  increases, while the volume-weighted  $\langle w_s \rangle_{\text{vol}}/c_s$  remains relatively constant. The gas  $\delta u_{\text{gas}}$  also continues to grow, but this is increasingly driven by the small volume of gas “caught up” in the filaments being rapidly accelerated by high-density dust.

the polytropic EOS after shocks, rather than allowing the entropy to increase (otherwise the box-averaged pressure and sound speed would increase in time without limit). In the linear regime, the different EOS modifies only an order-unity pre-factor in the RDI growth rate and we find qualitatively similar results in the simulation here.

In the saturated state, we find the gas turbulence and resulting gas density fluctuations are modestly suppressed for the stiffer EOS, as expected, but this is again an order-unity effect (note that turbulent Mach numbers are sub-sonic here). Further, the PDF of  $\rho_g/\rho_d$  is narrower in the  $\gamma = 5/3$  case than in the  $\gamma = 1$ .

## 5 CONCLUSIONS

In this paper, we present the first study of the non-linear regime of the acoustic RDI. We focus on the simple case of dust grains in a homogeneous medium, coupled via aerodynamic (Epstein) drag, with a constant differential acceleration between gas and dust. We find that the acoustic RDI grows robustly at all scales, eventually breaking up into internally generated turbulence and saturating at large amplitudes. The turbulence is highly anisotropic, with dust concentrated in filaments, plumes or jets along the direction of acceleration. Strongly non-linear structure including orbit crossings occur routinely in the dust, necessitating numerical simulations which can follow the velocity distribution function of the grains. We show the simulations can be conveniently characterized by three dimensionless numbers, and survey the parameter space to characterize the saturated states.

The linear growth rates and structure (e.g. wavenumbers and their “resonant angles”) of the fastest-growing modes agree with the predictions from linear theory (Hopkins & Squire 2018b). The resonant angles are sufficiently virulent to persist well into the non-linear state, and can be clearly seen in the turbulence. The behavior in the linear regime can be organized into three regimes based on the range of wavenumber  $k \langle c_s \rangle \langle t_s \rangle$  (“low,” “mid,” and “high”- $k$ ), and we find this division persists in the non-linear regime.

The mid and high- $k$  regimes seem qualitatively similar (but quantitatively distinct): the turbulence driven in the gas is sub-sonic, and only weakly compressible. Although the dust and gas local velocity dispersions reach rough equipartition in saturation, the dust density structure is strongly modified, with the aforementioned plumes and filaments appearing. This generates a distribution of  $\rho_d/\rho_g$  which has an approximate log-normal (or perhaps power-law-like in the tails) shape, with  $1\sigma$  dispersions reaching  $\sim 0.3 - 0.6$  dex (reaching orders-of-magnitude fluctuations, in the tails).

The low- $k$  regime is essentially defined by wavenumbers where the pressure gradient forces in equilibrium are weak compared to the bulk force exerted by dust on gas. This makes the gas more compressible, and it is driven by the dust into large density fluctuations, and even shocks. To leading order dust and gas densities are correlated, albeit with significant scatter at any  $\rho_g$ . The fastest-growing mode structures are distinct, with wavenumber aligned with the acceleration direction, producing long-wavelength “arcs” or “shells” in dust and gas.

In all cases, we note that the non-linear behavior is qualitatively different from the results of “passive” dust simulations, in which the dust is treated as a pure tracer population (i.e. the gas does not “feel” the dust), with externally-driven turbulence.

These simulations form a first step towards studying the effects of the acoustic RDI on astrophysical phenomena. Certainly, the large dust density and velocity fluctuations and non-linear, anisotropic concentrations produced, will alter critical properties such as dust-gas chemistry, dust growth and collision rates, extinction and effective/observable attenuation curves, and more. Future work will consider detailed applications to specific astrophysical environments – e.g. cool-star winds, AGN torii, and dense GMCs – but these require additional physics (e.g. radiative cooling, or global simulations with outflow boundaries) that break the scale-free nature of our studies here. While we work in dimensionless problem units here, in Hopkins & Squire (2018b) we discuss how these translate to physical units in the astrophysical environments mentioned above. For reference, the boundary between low- and mid- $k$  regimes (long and mid-wavelength modes) occurs around scales of  $\sim 0.001 - 0.1$  pc in GMCs,  $\sim 1 - 100$  au in AGN torii, and  $\sim 10^3 - 10^5$  km in cool-star wind environments, for typical parameters. In all cases, these are relatively small scales compared to those of the systems in question.

In this paper, in order to aid physical understanding, we simplified by assuming a single grain size in each simulation. This implies that quantities like the stopping time, resonant angle, and drift velocity are single-valued. In future work, we will explore the more physical case with a spectrum of grain sizes. We will also explore higher-order diagnostics, e.g. grain clustering and collision kernels. Finally, a wide variety of other RDIs remain to be explored in the nonlinear regime, with many (e.g. magnetohydrodynamical RDIs, or the epicyclic RDI) likely to have qualitatively different non-linear behavior and saturation mechanisms.

## ACKNOWLEDGMENTS

We would like to thank Stefania Moroianu for a number of helpful discussions. Support for PFH, JS, & ERM was provided by an Alfred P. Sloan Research Fellowship, NSF Collaborative Research Grant #1715847 and CAREER grant #1455342, and NASA grants NNX15AT06G, JPL 1589742, 17-ATP17-0214. Numerical calculations were run on the Caltech compute cluster “Wheeler,” allocations from XSEDE TG-AST130039 and PRAC NSF.1713353 supported by the NSF, and NASA HEC SMD-16-7592.

## REFERENCES

- Bai X.-N., Stone J. M., 2010a, *ApJ*, 722, 1437  
 Bai X.-N., Stone J., 2010b, *ApJ*, 722, L220  
 Carballido A., Stone J. M., Turner N. J., 2008, *MNRAS*, 386, 145  
 Cuzzi J. N., Hogan R. C., Bottke W. F., 2010, *Icarus*, 208, 518  
 Draine B. T., Salpeter E. E., 1979, *ApJ*, 231, 77  
 Federrath C., Klessen R. S., Schmidt W., 2008, *ApJ*, 688, L79  
 Hogan R. C., Cuzzi J. N., Dobrovolskis A. R., 1999, *Physical Review E*, 60, 1674  
 Hopkins P. F., 2014, GIZMO: Multi-method magneto-hydrodynamics+ gravity code  
 Hopkins P. F., Lee H., 2016, *MNRAS*, 456, 4174  
 Hopkins P. F., Squire J., 2018a, *MNRAS*, 479, 4681  
 Hopkins P. F., Squire J., 2018b, *MNRAS*, 480, 2813  
 Johansen A., Youdin A., Mac Low M.-M., 2009, *ApJ*, 704, L75  
 Lee H., Hopkins P. F., Squire J., 2017, *MNRAS*, 469, 3532  
 Pan L., Padoan P., 2013, *ApJ*, 776, 12  
 Pan L., Padoan P., Scalo J., Kritsuk A. G., Norman M. L., 2011, *ApJ*, 740, 6  
 Squire J., Hopkins P. F., 2018a, *ApJ*, 856  
 Squire J., Hopkins P. F., 2018b, *MNRAS*, 477, 5011  
 Trumpler R. J., 1930, *Publications of the Astronomical Society of the Pacific*, 42, 267  
 Youdin A. N., Goodman J., 2005, *ApJ*, 620, 459

## APPENDIX A: NUMERICAL LIMITATIONS IN THE HIGH-WAVENUMBER REGIME

In some simulations – in particular those at high dimensionless wavenumber,  $k \langle c_s \rangle \langle t_s \rangle$  – the RDI does not grow as expected from linear-theory, with the gas remaining laminar (or nearly so) over the duration of the simulation. We do not believe this to be a physical effect, but rather due to finite resolution and numerical dissipation/noise. We discuss the possible causes for this here, in order to motivate further study of this regime. The affected simulations are shown with gray text in Table 1 (recall that there are also some simulations, e.g.  $\mu 0.01 - \bar{a}1 - \bar{\epsilon}_d 0.1$ , that do not go turbulent because they are subsonic and in the mid- $k$  or high- $k$  regime, where growth rates are very low; see Hopkins & Squire 2018b).

A particular challenge for simulating the RDI in the high  $k \langle c_s \rangle \langle t_s \rangle$  regime is resolving the resonant angle. While we can always construct a box that resolves arbitrarily high  $k \langle c_s \rangle \langle t_s \rangle$  by changing the simulation parameters ( $\bar{a}$  and  $\bar{\epsilon}_d$ ), as shown in Hopkins & Squire (2018b), the linear growth rates become increasingly sharply peaked around the resonant angle (where  $\hat{\mathbf{k}} \cdot \mathbf{w}_{s,\text{eq}} = c_s$ ) with increasing  $k \langle c_s \rangle \langle t_s \rangle$ . More precisely, defining the largest mode in the box as  $k_0 = \xi / (\mu c_s \langle t_s \rangle)$  (where  $\xi > 1$  is required to be in the high- $k$  regime), the growth rate drops by orders of magnitude outside some width in mode angle,  $\Delta \cos \theta_k \sim \Delta \theta_k \sim \mu \xi^{-1/3} ((w_s)/c_s)^{-1}$  (in the high- $k$  regime). At finite resolution, any angular structure smaller than  $\Delta \theta \sim \Delta x / L_0 = N^{-1/3}$  will be unable to be resolved. At our fiducial resolution of  $N^{1/3} = 128$ , this means

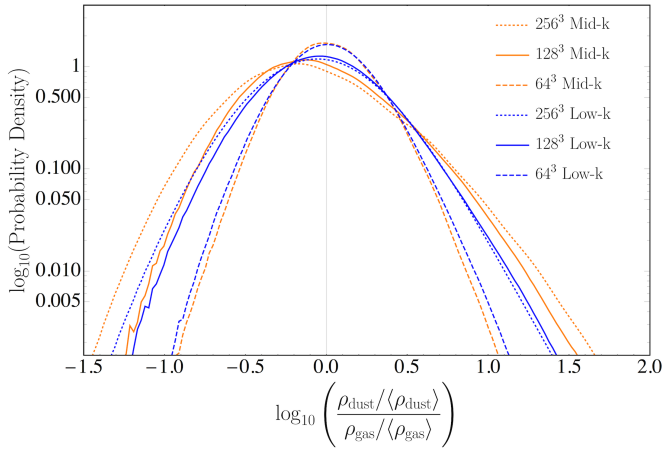


**Figure A1.** The volume weighted PDFs of dust density over gas density for the simulations  $\mu 0.01\text{-}\bar{a}1e4\text{-}\bar{\epsilon}_d 0.001$ ,  $\mu 0.01\text{-}\bar{a}100\text{-}\bar{\epsilon}_d 0.1$  and their high/low resolution counterparts  $\mu 0.01\text{-}\bar{a}1e4\text{-}\bar{\epsilon}_d 0.001\text{-HR/LR}$  and  $\mu 0.01\text{-}\bar{a}100\text{-}\bar{\epsilon}_d 0.1\text{-HR/LR}$ . In the majority of our simulations, we have  $128^3$  dust and gas particles. In order to test the effects of resolution on our results, we have run and examined two simulations with  $256^3$  dust and gas particles and two with  $64^3$ . The particular parameters of these simulations (i.e.  $\mu$ ,  $\bar{\epsilon}$ , and  $\bar{a}$ ) are identical to those of  $\mu 0.01\text{-}\bar{a}1e4\text{-}\bar{\epsilon}_d 0.001$  and  $\mu 0.01\text{-}\bar{a}100\text{-}\bar{\epsilon}_d 0.1$ . We find that our results seem relatively well converged at  $128^3$ . The low-density tails of the PDFs here are not sampled quite as well in the  $128^3$  simulations as in the  $256^3$ , while on the high-density end the PDFs are better resolved. In the low resolution,  $64^3$  simulations, the high and low density regions are more poorly sampled, and the simulations fail to accurately capture the non-Gaussian structure of the PDFs. Other statistics associated with the saturated state of the simulations are also mostly unchanged when increasing the resolution (c.f. Table 1).

we can only barely resolve resonant angles in the high- $k$  regime for marginally high- $k$  boxes ( $\xi \sim 1$ ), relatively low  $\langle w_s \rangle / c_s \sim 1 - 10$ , and relatively high  $\mu \sim 0.1$ . Examination of the parameters in Table 1 shows that almost all simulations that fail to become turbulent do indeed have very narrow RDI resonances. Unfortunately, this numerical issue is difficult to overcome (e.g. fixed-grid-based codes almost certainly face the same issues) and even significant increases in resolution allow only modest gains in the resolvable resonant angles (and thus the  $k \langle c_s \rangle t_s$  that is possible to simulate). Two-dimensional simulations, which allow much higher resolutions, could thus be particularly helpful for study of the high- $k$  regime.

There is another numerical issue, again primarily affecting the high- $k$  regime, which is more specific to the Lagrangian finite-volume method used here. In the linear regime, at increasing  $k$ , the back-reaction from drag becomes an increasingly small perturbation compared to pressure forces (as  $\nabla P \sim kP$ ). Non-linearly, as discussed in § 3, this translates to the predicted  $\delta u_{\text{gas}} / c_s$ : again defining  $k_0 = \xi / (\mu c_s \langle t_s \rangle)$ , then in the high- $k$  regime, we see that  $\delta u_{\text{gas}} / c_s \sim \mu \xi^{-2/3}$ , which is very small (see Eq. 8). It is well-known that both finite-volume and Lagrangian numerical hydrodynamics methods have difficulty accurately capturing very low Mach number, nearly-incompressible turbulence: the Riemann solver introduces numerical diffusion and the constant re-arrangement of the grid introduces “remeshing noise,” which launches sound waves, both of which make it difficult to follow highly-subsonic effects. In Hopkins (2014), we show specifically for the numerical methods

here that sub-sonic effects can be numerically over-damped below turbulent Mach numbers  $\ll 0.01$ .

To capture RDI-induced turbulence at such low  $\delta u_{\text{gas}} / c_s$ , other, lower-noise, numerical methods may be required. Note that in every case tested where the instabilities failed to grow, either the predicted  $\delta u_{\text{gas}} / c_s \ll 0.01$ , or the resonant angle was unresolved (usually both).

## APPENDIX B: SIMULATION RESOLUTION

In Fig. A1, we illustrate the dependence of the density PDFs on resolution for the low- $k$  and mid- $k$  simulations, which are not strongly affected by the numerical difficulties discussed above. We see that the differences between the  $128^3$  and  $256^3$  simulations are minimal, although, perhaps unsurprisingly, the highest and lowest  $\rho_d / \rho_g$  are somewhat unresolved at  $128^3$ . At  $64^3$  the PDFs look significantly more Gaussian, illustrating that aspects of the turbulence are not being correctly resolved. We note, however, that the general characteristics of the RDI – e.g. the resonant angle and general structure of the instability – look very similar at all three resolutions (not shown).